

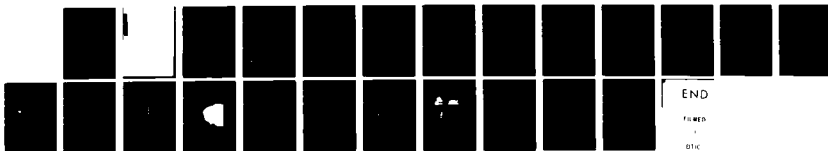
AD-A121 043

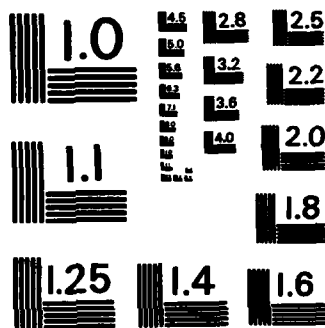
MEASUREMENTS OF LASER COUPLING AND PLASMA PROFILES IN
LONGER-SCALELENGTH PLASMAS(U) NAVAL RESEARCH LAB
WASHINGTON DC M J HERBST ET AL. 30 SEP 82 NRL-MR-4893
F/G 20/5

1/1

UNCLASSIFIED

NL





MICROCOPY RESOLUTION TEST CHART
NATIONAL BUREAU OF STANDARDS - 1963 - A

AD A 121043

SECURITY CLASSIFICATION OF THIS PAGE (When Data Entered)

REPORT DOCUMENTATION PAGE		READ INSTRUCTIONS BEFORE COMPLETING FORM
1. REPORT NUMBER NRL Memorandum Report 4893	2. GOVT ACCESSION NO. AD-A121043	3. RECIPIENT'S CATALOG NUMBER
4. TITLE (and Subtitle) MEASUREMENTS OF LASER COUPLING AND PLASMA PROFILES IN LONGER-SCALELENGTH PLASMAS		5. TYPE OF REPORT & PERIOD COVERED
7. AUTHOR(s) M.J. Herbst, P.G. Burkhalter, J. Grun,* S.P. Obenschain, J.A. Stamper, F.C. Young, E.A. McLean, B.H. Ripin, and R.R. Whitlock		6. PERFORMING ORG. REPORT NUMBER
9. PERFORMING ORGANIZATION NAME AND ADDRESS Naval Research Laboratory Washington, D.C. 20375		8. CONTRACT OR GRANT NUMBER(s)
11. CONTROLLING OFFICE NAME AND ADDRESS U.S. Department of Energy Washington, D.C. 20545		10. PROGRAM ELEMENT, PROJECT, TASK AREA & WORK UNIT NUMBERS DPE AI08-79DP 40092(172) 47-0859-0-2
14. MONITORING AGENCY NAME & ADDRESS (if different from Controlling Office)		12. REPORT DATE September 30, 1982
		13. NUMBER OF PAGES 22
		15. SECURITY CLASS. (of this report) UNCLASSIFIED
		15a. DECLASSIFICATION/DOWNGRADING SCHEDULE
16. DISTRIBUTION STATEMENT (of this Report) Approved for public release; distribution unlimited.		
17. DISTRIBUTION STATEMENT (of the abstract entered in Block 20, if different from Report)		
18. SUPPLEMENTARY NOTES This paper was prepared for presentation at the 12th Annual Anomalous Absorption Conference to be held in Santa Fe, New Mexico, May 10-13, 1982. *Present Address: Mission Research Corp., Alexandria, VA 22312		
19. KEY WORDS (Continue on reverse side if necessary and identify by block number) Laser-matter interaction Plasma instabilities X-ray spectroscopy Plasma diagnostics		
20. ABSTRACT (Continue on reverse side if necessary and identify by block number) Novel configuration of our two-beam laser allows laser-coupling experiments to be performed in longer-scalelength plasmas ($L_n \approx 250-600 \mu m$ at $n_c/10$), which better simulate reactor-sized pellet plasmas. Preliminary observations show increased backscatter, as expected, but also reveal large re- ductions in $2\omega_0$ and high-energy x-ray emissions. The latter may indicate lessened importance of resonance absorption in longer-scalelength plasmas. Measurements of plasma profiles are at least as important as coupling measurements in these experiments and we show new diagnostic techniques (Continued)		

DD FORM 1473
1 JAN 73EDITION OF 1 NOV 65 IS OBSOLETE
S/N 0102-014-6601

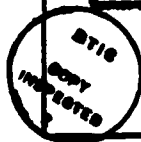
SECURITY CLASSIFICATION OF THIS PAGE (When Data Entered)

20. ABSTRACT (Continued)

based upon tracer-dot methods. These include the first techniques available for velocity profile measurement, as well as an improved x-ray spectroscopic method for density and temperature profile measurement.

X

Accession For	
NTIS GRA&I	<input checked="" type="checkbox"/>
DTIC TAB	<input type="checkbox"/>
Unannounced	<input type="checkbox"/>
Justification	
By	
Distribution/	
Availability Codes	
Dist	Avail and/or Special



CONTENTS

I.	INTRODUCTION	1
II.	PRELIMINARY LONGER-SCALELENGTH EXPERIMENTS	2
III.	PLASMA PROFILE MEASUREMENTS	3
IV.	STATUS REPORT	5
V.	ACKNOWLEDGMENTS	5
	REFERENCES	5

MEASUREMENTS OF LASER COUPLING AND PLASMA PROFILES IN LONGER-SCALELENGTH PLASMAS

I. INTRODUCTION

To maximize applicability of current laser-plasma coupling experiments to high-gain laser fusion, these experiments should include three very important characteristics. First, laser-target coupling studies should be performed in plasmas with longer density, temperature, and velocity scalelengths to minimize the extrapolation which must be made from present experiments to the multimillimeter-scalelength plasmas anticipated for high-gain pellets. Second, measurements should be made over a wide range of scalelengths to provide a number of benchmarks for the plasma and hydrodynamics codes which are used to make the extrapolation. This is important because the absorption physics in long-scalelength plasmas may be qualitatively (as well as quantitatively) different from that in short-scalelength plasmas; the various processes which determine absorption efficiency depend differently on plasma scalelengths, and the processes which determine the absorption efficiency in short-scalelength plasmas might not be the same processes which are most important in long-scalelength plasmas. Finally, it is important that a complete set of plasma scalelength measurements be made in these experiments. If one measures absorption or scattered light and does not specify the scalelengths, free parameters are available which may be used in a hydro-code calculation to fit the measurements; for example, the flux limiter may be varied (which alters the plasma profiles) to obtain agreement with the experiment. In this case, the physics assumptions in the calculation are not being properly tested, and no confidence is developed in the ability of the hydro-code to predict laser-target coupling in reactor-sized plasmas.

Standard measurements of laser coupling with solid targets exhibit weaknesses on all three points. As illustrated in Fig. 1, these generally involve focusing the laser to a small spot in order to obtain the higher intensities of interest for high-gain scenarios. Planar geometry, rather than spherical, is commonly used because somewhat longer plasma scalelengths can be produced with fixed laser power and intensity. Even so, scalelengths produced by a small focal spot are still much shorter than reactor scalelengths because of the divergent flow of plasma from the finite planar spot. Moreover, variations of laser intensity and plasma scalelength cannot be made independently. If the laser power is varied to change the irradiance at constant spot size, the plasma scalelength varies also; if laser spot size is varied to control plasma scalelength, laser irradiance and focal quality change as well. Measurements of density and temperature profiles have not been made routinely in these experiments, and techniques for velocity profile measurement have not been developed.

Significant physics results have been obtained in previous experiments designed to address laser coupling in longer scalelength plasmas; these experiments have also had limitations. Using underdense gas targets to eliminate complicating effects due to the presence of a critical surface, investigators have made positive identifications of stimulated Brillouin backscatter¹⁻⁴ and sidescatter⁵ and of stimulated Raman scattering.⁶ They have also observed the saturation of Brillouin backscatter⁷⁻⁹ and sidescatter.⁵ Measurements^{4,10} and calculations¹¹ suggest that coupling to these plasmas is dependent upon the dynamics of ionization and heating waves, as well as upon the hydrodynamic expansion lateral to the

laser axis; thus, the dynamics of the gas target plasmas are as complicated as the dynamics of solid target plasmas but are less similar to the dynamics of reactor pellet plasmas. Furthermore, the scalelengths in these underdense gas targets are often so long that they can be treated by the theory of parametric instabilities in homogeneous plasmas; therefore, one does not check the inhomogeneous theory of relevance to reactor pellets. More recent experiments with inhomogeneous, overdense gas targets¹²⁻¹⁴ overcome this latter problem. However, the important effect of the flow velocity gradient along the laser axis is still not present.

At NRL, longer-scalelength solid-target experiments in progress are designed to include effects of flow velocity gradients while overcoming the abovementioned deficiencies of standard solid-target experiments. To produce longer scalelength plasmas, two separate beams from our Nd laser ($\lambda = 1.054 \mu\text{m}$) may be focused in different planes, as shown in Fig. 2. One beam, operating with up to 250 J in a 3-5 ns pulse, is brought to a large diameter ($\approx 1 \text{ mm}$) spot at the target to produce plasmas with density scalelengths $L_n \equiv n/\nabla n$ of 250-600 μm at $n_c/10$. The second beam is tightly focused inside the first to give the high intensities of interest for laser-plasma coupling experiments. By reducing the pulse duration of the second beam to $\tau_L < 0.5 \text{ ns}$ (with laser energies as high as 25 J), we can minimize the perturbation to the long-scalelength hydrodynamic flow of the first beam that is caused by this higher intensity region. Both high intensity and long scalelength can be achieved in these experiments, and the two parameters may be varied independently since the scalelength is determined by the larger spot size and the intensity by the smaller spot size. This new method for performing longer-scalelength coupling experiments has evolved from prepulse techniques pioneered by NRL in the mid-1970's.¹⁵ As will be discussed later in this paper, we are developing new plasma diagnostic techniques to make improved measurements of density and temperature profiles, as well as the first measurements of velocity profiles.

II. PRELIMINARY LONGER-SCALELENGTH EXPERIMENTS

Preliminary observations of laser-plasma coupling have been made using this two-beam configuration to produce longer scalelengths. As indicated in Fig. 3, a significant increase in backscatter through the lens is observed when the large-focus beam is combined with the tightly focused beam; this occurs both for long pulse length and short pulse length operation of the higher intensity beam, although the maximum intensity achievable in the former case is lower due to laser protection considerations. Despite the large increase observed in backscatter from the carbon targets used in these experiments, the maximum backscatter is 10 percent; thus, the backscatter accounts for only a small fraction of the incident energy. Measurements of scattered light at other angles, which have not yet been reduced, may alter this picture.

While the increase in backscatter in these preliminary longer-scalelength experiments was entirely predictable from parametric instability theory,¹⁶ two other observations are more surprising. Time-integrated images of second-harmonic emission, taken at 90° to the incident laser axis, are shown in Fig. 4. When a single high-intensity beam is focused on a carbon target, as in the left hand image, a localized region of copious $2\omega_0$ emission is observed. When this same high-intensity beam is incident upon the longer scalelength plasma set up by the large-focus beam, the intensity of the $2\omega_0$ emission is not detectable, as in the right-hand image.

The second surprising observation is in the x-ray emission. Time integrated spectra of 1-50 keV x-rays are obtained with arrays of PIN diodes and photomultiplier-scintillator detectors. With the single high-intensity beam incident upon a carbon target, x rays in the 10-50 keV spectral range are easily detected, as indicated in Fig. 5. However, with the same high-intensity beam incident upon the longer scalelength plasma, the intensity of x rays in this spectral region falls below detection thresholds (see Fig. 5). The upper bounds on the x-ray flux at 50 and 20 keV represent reductions from the single-beam case by factors of at least 30 and 1000, respectively! These reductions are consistent with observations made in longer-scalelength gas-jet targets at KMS.¹⁴

At least two explanations might be offered to account for the observations of $2\omega_0$ and energetic x-ray emission. First, a longer scalelength near critical density may directly reduce the importance of resonance absorption; this could explain the disappearance of both $2\omega_0$ emission and high-energy x-rays, and would indicate that the experimental conditions are such that the relative importance of various absorption processes is changing. The observations may also be explained by a reduced laser intensity at the critical surface, due to increased inverse Bremsstrahlung absorption or Brillouin scatter in the underdense plasma. The increased reflectivity through the lens in these preliminary experiments is insufficient to account for this, but measurements of scattered light at other angles, which have not yet been reduced, may alter the picture.

III. PLASMA PROFILE MEASUREMENTS

As mentioned above, measurements of plasma density, temperature, and velocity profiles are at least as important in these experiments as measurements of absorbed energy, scattered light, and x-rays. Without these measurements, scalelengths in hydrocodes may be varied to fit the experimental observations, and our confidence in the ability of these codes to extrapolate the physics correctly to reactor conditions is not increased.

To overcome the deficiency of previous coupling experiments, NRL is developing new methods for measurement of plasma profiles. All of these new methods have evolved from a technique presented at the 1981 Anomalous Absorption Meeting, which allowed the first visualizations of material flowlines from laser-irradiated targets.¹⁷ We use a special target, as shown in Fig. 6, which has Al tracer dots embedded within a polystyrene (CH) substrate. Here, the dots are $25\text{ }\mu\text{m}$ in diameter and are spaced by $50\text{ }\mu\text{m}$ center-to-center. Regions of Al flow from each of the dots are easily identified as tracks of stronger emissivity in pinhole-camera images of x-ray emission above 1 keV, because the Al line emission in this spectral region is much stronger than either the C or H continuum emission.

Examples of flow visualizations obtained in this way are shown in Fig. 7. These three images, obtained with different-sized pinholes on a single shot, show tracks of stronger volume emissivity resulting from the Al dots. Images obtained with smaller pinholes provide better spatial resolution, while those obtained with larger pinholes give greater sensitivity and allow visualization of the flow further from the target. A more thorough treatment of the flow patterns may be found in Ref. 17; the one property relevant to the present discussion is the distinctness of the streamlines. Since these x-ray images are time-integrated over the 4-nsec x-ray pulsewidth (FWHM), the absence of smearing of the streamlines suggests that we are in a nearly steady flow regime. Further experimental evidence for this flow condition is obtained from streaked images of $3\omega_0/2$ emission, which imply a nearly stationary $n_c/4$ surface.¹⁸

If we are, in fact, in a steady flow regime, we may use the flow visualizations in conjunction with a measured density profile to infer the fluid velocity profile in the plasma. As indicated in Fig. 8, the method relies upon the steady-state mass conservation equation, which tells us that the product of the density n in a streamtube, the cross-sectional area A of the streamtube, and the fluid velocity v in the streamtube is a constant, C . If we measure the density profile by interferometry or some other technique, and we obtain the area A from the flow visualizations, we need only to evaluate the constant C in order to obtain absolute values for the velocity. (Relative values may be obtained without C .) Experimentally, we may obtain C by imposing a boundary condition far from the target where the velocity has reached a constant value; in this region, we equate the velocity with that measured far from the target by time-of-flight ion detectors.

Data from a proof-of-principle experiment have been reduced using this model, as shown in Fig. 9. The density profile obtained interferometrically shows a $1/z^2$ dependence of the density with distance z far from the target (bottom of Fig. 9). In this same region, the flow visualizations show a spherically divergent flow, giving A proportional to z^2 . Since the product of density and area is constant in this region, the model of Fig. 8 implies that the flow velocity is constant (top of Fig. 9); it is in this

region that we equate the velocity to that measured in the far field by ion detectors. In closer to the target, the density variation changes and we begin to infer a change of the flow velocity from its far-field value. Interestingly, the region of nearly constant velocity extends inward approximately to the $n_e/10$ surface. This could explain the fact that Brillouin scatter from solid targets often seems to emanate from this lower density region¹⁵; velocity gradients may stabilize the Brillouin process at higher density. To infer the velocity profile for higher densities than $0.3 n_c$, the limit of the $3\omega_0$ interferometric probe under these conditions, a technique for measuring the higher densities closer to the target is needed.

To access higher densities, we are developing an improved x-ray spectroscopic method, as illustrated in Fig. 10.¹⁹ Here, a polystyrene target with a single embedded Al spot is used, but now the Al is serving as a localized source of x-ray line emission for spectroscopic diagnosis. The Al line radiation is collected by an imaging spectrograph with the entrance slit oriented to give spatial resolution along the laser axis. This technique has three major advantages over standard laser-plasma spectroscopy (where the target is entirely Al). First, emission is obtained only from a known volume within the plasma, rather than by integrating along the diagnostic line-of-sight through regions of differing density and temperature; thus, local measurements are made directly, without the need for deconvolution. Second, effects of plasma reabsorption of the emitted radiation are greatly reduced, particularly if a higher Z spot is embedded in a lower Z target; this simplifies interpretation of measured spectra. Third, the reduced size of the emitter leads to better spectral resolution because source broadening of the detected radiation is reduced.

To demonstrate this third point, data obtained with this new technique are compared with standard spectroscopic data in Fig. 11. In Fig. 11A, a set of pinhole images from an Al target show that a large volume of plasma participates in the x-ray emission, as one would expect. In contrast, pinhole images from a single-spot target show a well-confined channel of Al line emission within a larger-diameter region of plastic continuum emission, as seen in Fig. 11C. The result of this reduced emitter diameter is that better spectral resolution is seen in the spectrum obtained with a spotted target, in Fig. 11D, than is seen in the standard spectrum of Fig. 11B. More details on this new technique may be found in Ref. 19.

With this improved spectral resolution, one expects that better comparisons between data and spectroscopic models will be made and that these will lead to improved density and temperature measurements.²⁰ A standard technique for plasma density measurement relies upon the ratio between the He-like intercombination line (He 2^3P) and the He-like resonance line (He- α)²¹; the measured variation of this ratio with distance z from the target is shown in the left-hand graph of Fig. 12. Collisional-radiative equilibrium models indicate that this ratio should fall monotonically with increasing density except for plasma opacity effects very near to the target.²² For $z \geq 200 \mu\text{m}$, this expected behavior is observed and leads to the solid portion of the density profile curve in the right-hand graph of Fig. 12; this yields densities up to $0.5 n_c$. For $z < 200 \mu\text{m}$, we observe an apparent levelling off or even an increase in the He 2^3P /He- α ratio. At this time, we believe that this is due to interfering spectral lines which nearly underlie the He 2^3P line and increase relative to it as the density increases. In previous experiments, the spectral resolution was not sufficient to distinguish these from the intercombination line; with our greater spectral resolution, we are on the verge of resolving these lines. Were we to naively apply previous models to the apparently saturated line ratio, we would obtain a density shelf at 5×10^{20} electrons/cm³ for $z < 200 \mu\text{m}$. In fact, we believe the He 2^3P /He- α ratio continues to decrease, as indicated by the speculative dashed curve. This would imply higher densities, as shown by the dashed curve in the right-hand graph of Fig. 12; densities up to $2n_c$ should be accessible with this technique. We are currently working on eliminating the problem by using a more detailed model, which should result in reliable measurement of these higher densities.

For temperature determinations, we rely upon intensity ratios between He-like and H-like Rydberg lines. Intensity variations of three of the stronger lines with distance from the target are shown in the left-hand side of Fig. 12, and temperatures inferred from the ratios of these lines are shown in the

right-hand graph of the same figure. For $z < 200 \mu\text{m}$, the temperatures are speculative because the inferred temperatures are dependent upon the inferred densities which are speculative at this region, as discussed above.

One final note concerns a new, untested idea to improve the velocity profile measurement. The method described earlier in Figs. 8 and 9 suffered from three drawbacks: (1) it required the assumption of steady state, (2) it required simultaneous measurement of the density profile, and (3) it gave only a time-averaged velocity profile. To overcome all three of these problems, we propose the use of layered tracer dots, as shown in Fig. 13. By making the tracer dot from alternating layers of two materials which have distinguishable x-ray emissivity, we should obtain a direct measure of the velocity profile with time resolution. We may follow the front of each of these layers as it transits the blowoff plasma by imaging the x rays onto the slit of a streak camera; the resultant z, t curve of the front directly measures the velocity profile. The time evolution of this profile is obtained from the multiple layers; each interface gives us the velocity profile at one time.

IV. STATUS REPORT

To summarize, studies of laser coupling in longer-scalelength plasmas which better simulate reactor plasmas are underway at NRL, as indicated in Fig. 14. Preliminary observations do show increased backscatter, as expected. The concomitant decrease in second-harmonic and high-energy x-ray emissions may indicate that we are entering a new physics regime where longer scalelengths are reducing the relative importance of resonance absorption.

Because we realize that these experiments are best used to benchmark the codes that are used for scaling to reactor-sized plasmas, we believe that measurements of plasma profiles are at least as important as measurements of laser-target coupling. We have demonstrated one technique and proposed a second improved technique for velocity profile measurement; these are the first techniques available for measurement of the velocity profile, which is important in evaluating parametric instability mechanisms. In addition, we have demonstrated an improved method for x-ray spectroscopic measurements, and we are developing the necessary improved models for extraction of plasma density and temperature. We hope to make more definitive statements on laser-coupling and profile measurements in longer-scalelength plasmas in the near future.

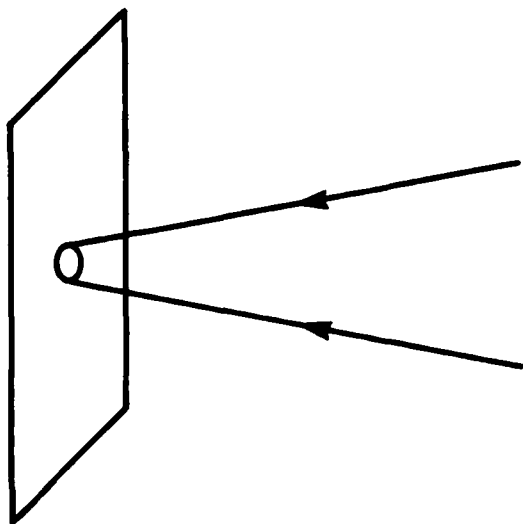
V. ACKNOWLEDGMENTS

The development of x-ray spectroscopy as described in Sec. III would not have been possible without the computational support of Dr. D. Duston. We also wish to acknowledge the expert technical assistance of M. Fink, N. Nocerino, and E. Turbyfill. This work was supported by the U.S. Department of Energy and Office of Naval Research.

REFERENCES

1. J.J. Turechek and F.F. Chen, Phys. Rev. Lett. **36**, 720 (1976).
2. R. Massey, K. Berggren, and Z.A. Pietrzyk, Phys. Rev. Lett. **36**, 963 (1976).
3. A.A. Offenberger, M.R. Cervenak, A.M. Yam, and A.W. Pasternak, J. Appl. Phys. **47**, 1451 (1976).
4. N.H. Burnett, H.A. Baldis, G.D. Enright, M.C. Richardson, and P.B. Corkum, J. Appl. Phys. **48**, 3727 (1977).
5. M.J. Herbst, C.E. Clayton, and F.F. Chen, J. Appl. Phys. **51**, 4080 (1980).

6. R.G. Watt, R.D. Brooks, and Z.A. Pietrzyk, Phys. Rev. Lett. **41**, 170 (1978).
7. A. Ng, L. Pitt, D. Salzmänn, and A.A. Offenberger, Phys. Rev. Lett. **42**, 307 (1979).
8. M.J. Herbst, C.E. Clayton, and F.F. Chen, Phys. Rev. Lett. **43**, 1591 (1979).
9. Z.A. Pietrzyk and T.N. Carlstrom, App. Phys. Lett. **35**, 681 (1979).
10. M.J. Herbst, C.E. Clayton, W.A. Peebles, and F.F. Chen, Phys. Fluids **23**, 1319 (1980).
11. N.H. Burnett and A.A. Offenberger, J. Appl. Phys. **45**, 2155 (1974).
12. F.J. Mayer, G.E. Busch, C.M. Kinzer, and K.G. Estabrook, Phys. Rev. Lett. **44**, 1498 (1980).
13. A.A. Offenberger and A. Ng, Phys. Rev. Lett. **45**, 1189 (1980).
14. J.A. Tarvin, F.J. Mayer, D.C. Slater, G.E. Busch, G. Charatis, T.R. Pattinson, R.J. Schroeder, and D. Sullivan, Phys. Rev. Lett. **48**, 256 (1982).
15. B.H. Ripin and E.A. McLean, Appl. Phys. Lett. **34**, 809 (1979) and references contained therein.
16. C.S. Liu, M.N. Rosenbluth, and R.B. White, Phys. Fluids **17**, 1211 (1974).
17. M.J. Herbst and J. Grun, Phys. Fluids **24**, 1917 (1981).
18. M.J. Herbst, J.A. Stamper, R.H. Lehmborg, R.R. Whitlock, F.C. Young, J. Grun, and B.H. Ripin, to appear in Proceedings of the 1981 Topical Conference on Symmetry Aspects of Inertial Fusion Implosions, ed. by S. Bodner, NRL.
19. M.J. Herbst, P.G. Burkhalter, R.R. Whitlock, J. Grun, and M. Fink, NRL Memorandum Report 4812, 1982. (to appear in Rev. Sci. Inst.).
20. P.G. Burkhalter, M.J. Herbst, D. Duston, R.R. Whitlock, and J. Grun, Proceedings of 1982 IEEE International Conference on Plasma Science and NRL Memorandum Report (to be published).
21. V.A. Boiko, S.A. Pikuz, and A. Ya. Faenov, J. Phys. B **12**, 1889 (1979).
22. D. Duston and J. Davis, Phys. Rev. **21A**, 1664 (1980).



$$E \leq 250 \text{ J}$$

$$t = 3\text{-}5 \text{ ns}$$

$$f/6, d_{50} \approx 80 \mu\text{m}$$

$$I \leq 10^{15} \text{ W/cm}^2$$

$$L_n (n_c/10) \leq 200 \mu\text{m}$$

Fig. 1 — Standard arrangement for laser-coupling experiments uses a tightly focused beam to achieve high intensity. At NRL, a single beam with 250 J in 3-5 ns can be focused to 80 μm diameter spot (50% energy content) by an $f/6$ lens, giving incident intensities up to 10^{15} W/cm^2 . In this case, plasmas can be generated with density gradient scalelengths at $n_c/10$ which just exceed 200 μm .

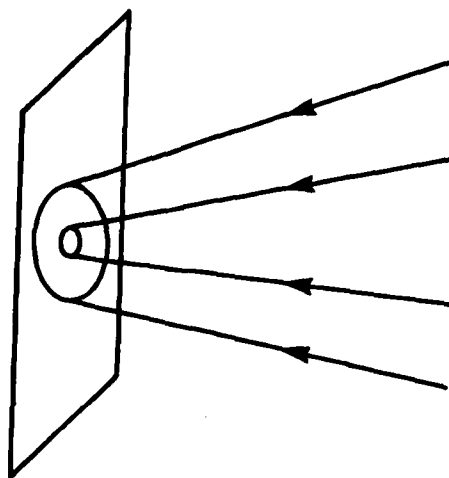


Fig. 2 — Novel configuration of two-beam laser allows production of longer-scalelength plasmas for coupling experiments. One beam with 3-5 nsec pulselength is brought to large focal diameter (≈ 1 mm) to produce longer scalelengths ($L_n \approx 250-600 \mu m$ at $n_c/10$), while a second beam is tightly focused within the first to produce higher intensities of interest. The pulselength of the high-intensity beam may be shortened to minimize its perturbation to the long-scalelength flow.

3-7 FOLD BACKSCATTER INCREASES AT MID- 10^{13} (5 ns) AND MID- 10^{14} (<0.5 ns) WHEN LARGE-FOCUS BEAM PRESENT

Fig. 3 — Summary of preliminary backscatter observations.

$2\omega_0$ IMAGES: STANDARD vs. LONGER SCALELENGTH

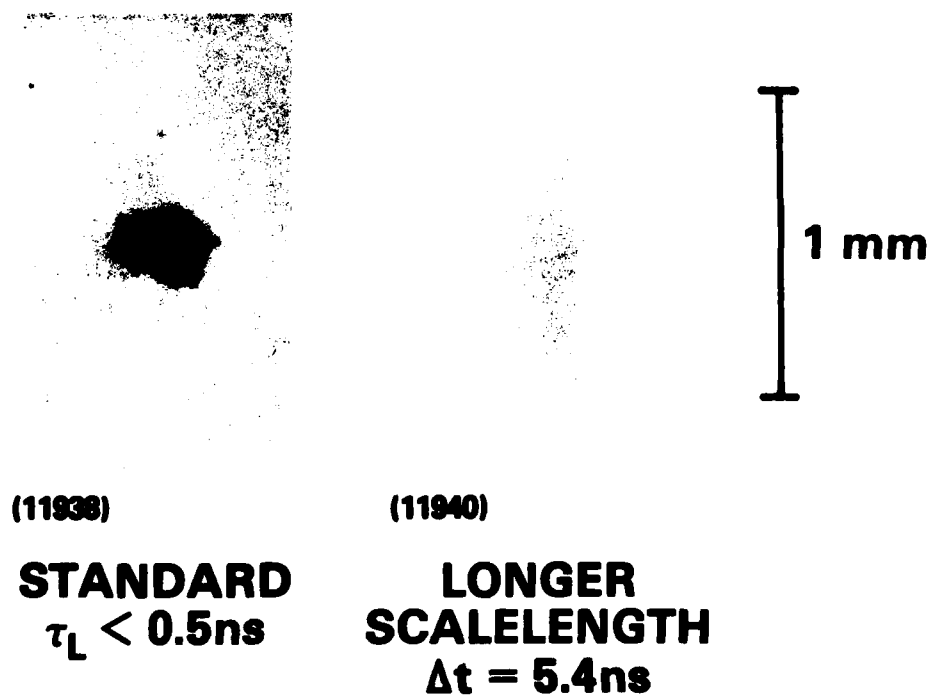


Fig. 4 — Comparison of time-integrated images of second harmonic emission for two modes of operation. The laser is incident from the left and the images are negatives. With a single high-intensity beam, the image on the left shows copious $2\omega_0$ emission. When the same high-intensity beam is focused into a longer-scalelength plasma, as shown in Fig. 2, the $2\omega_0$ emission disappears. The delay of the short-pulse, high intensity beam is 5.4 nsec after the peak of the longer pulse.

HIGH-ENERGY X-RAYS: STANDARD vs. LONGER SCALELENGTH

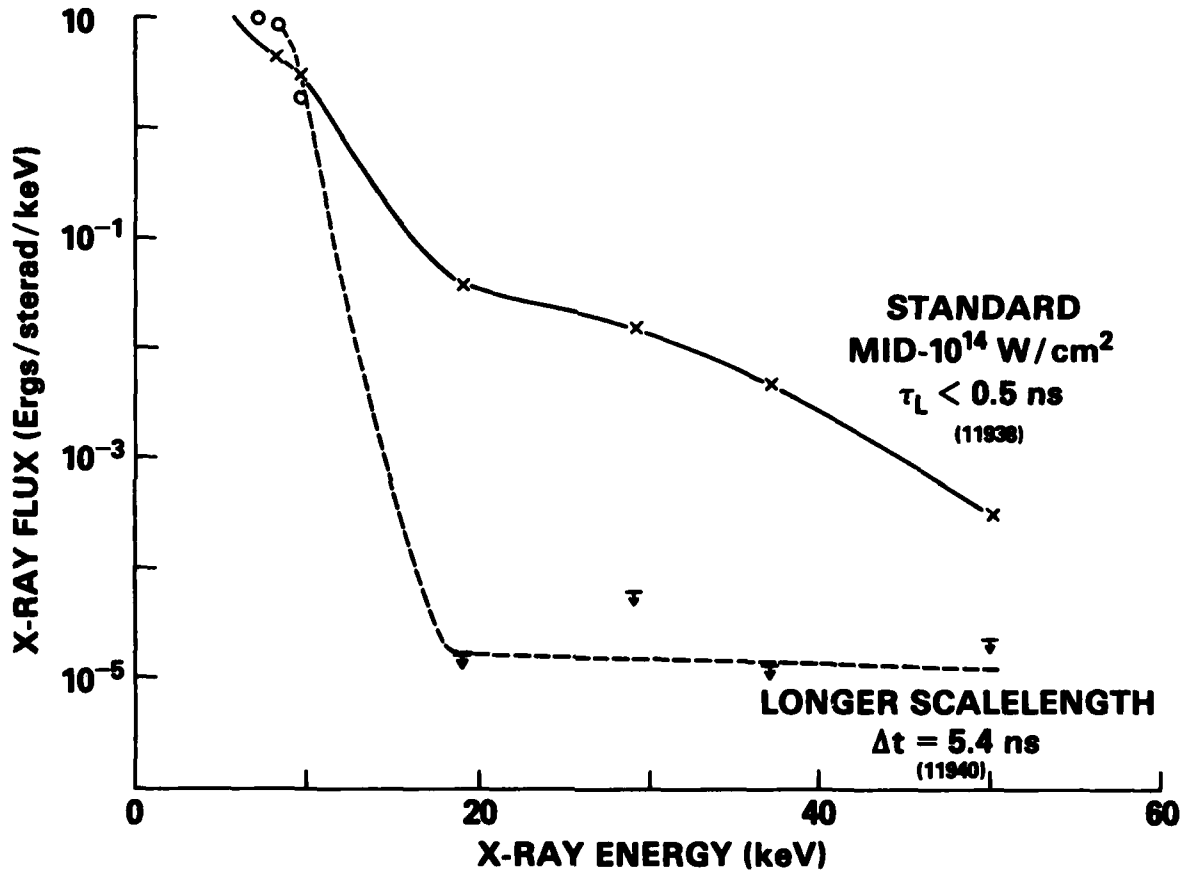


Fig. 5 — Comparison of high-energy x-ray spectra for two modes of operation. With a single, short-pulse, high-intensity beam, an x-ray tail corresponding to $T_h \approx 7 \text{ keV}$ is observed. This tail falls below the detection threshold for a long-scalelength target plasma. The delay of the short-pulse, high-intensity beam is 5.4 nsec after the peak of the longer pulse.

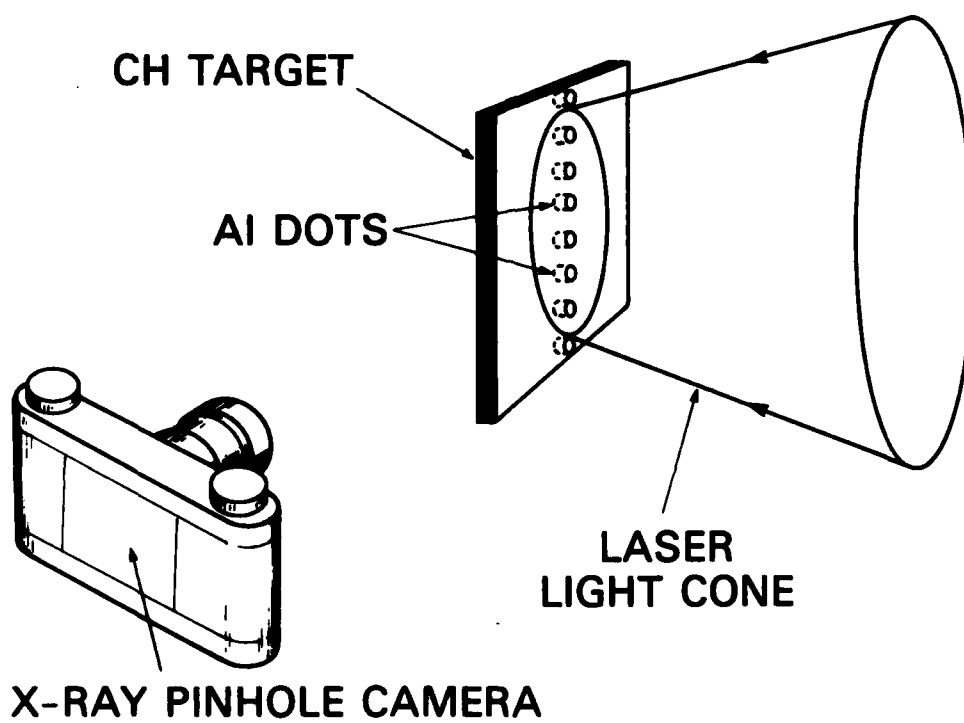


Fig. 6 — Schematic illustration of the experimental arrangement for visualization of hydrodynamic flows.

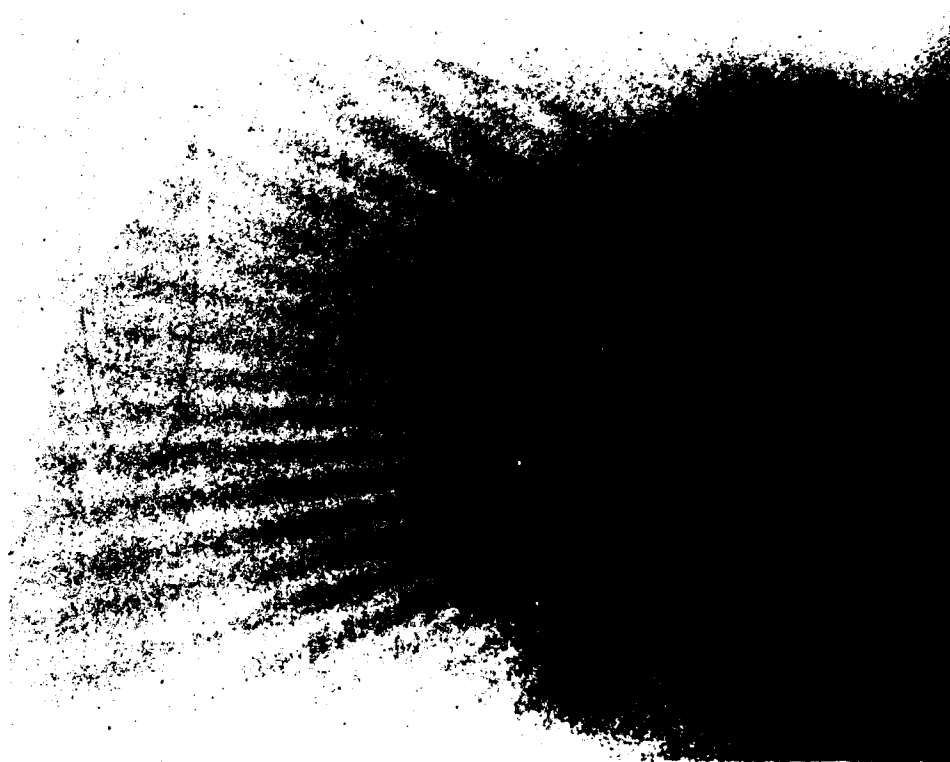


Fig. 7 — Time integrated images of x-ray emission obtained for single laser shot with 13, 28, and 54 μm diameter pinholes. Laser is incident from left, and images are negatives. Camera filter is nominally 15 μm thick Be. 230 J of laser energy is focused to 940 μm diameter spot (90% energy content) to give $I_0 \approx 8 \times 10^{12} \text{ W/cm}^2$ on 50 μm thick CH target.

STEADY-STATE MASS CONSERVATION

$$n A v = \text{constant}, C$$

$$v = \frac{C}{nA}$$

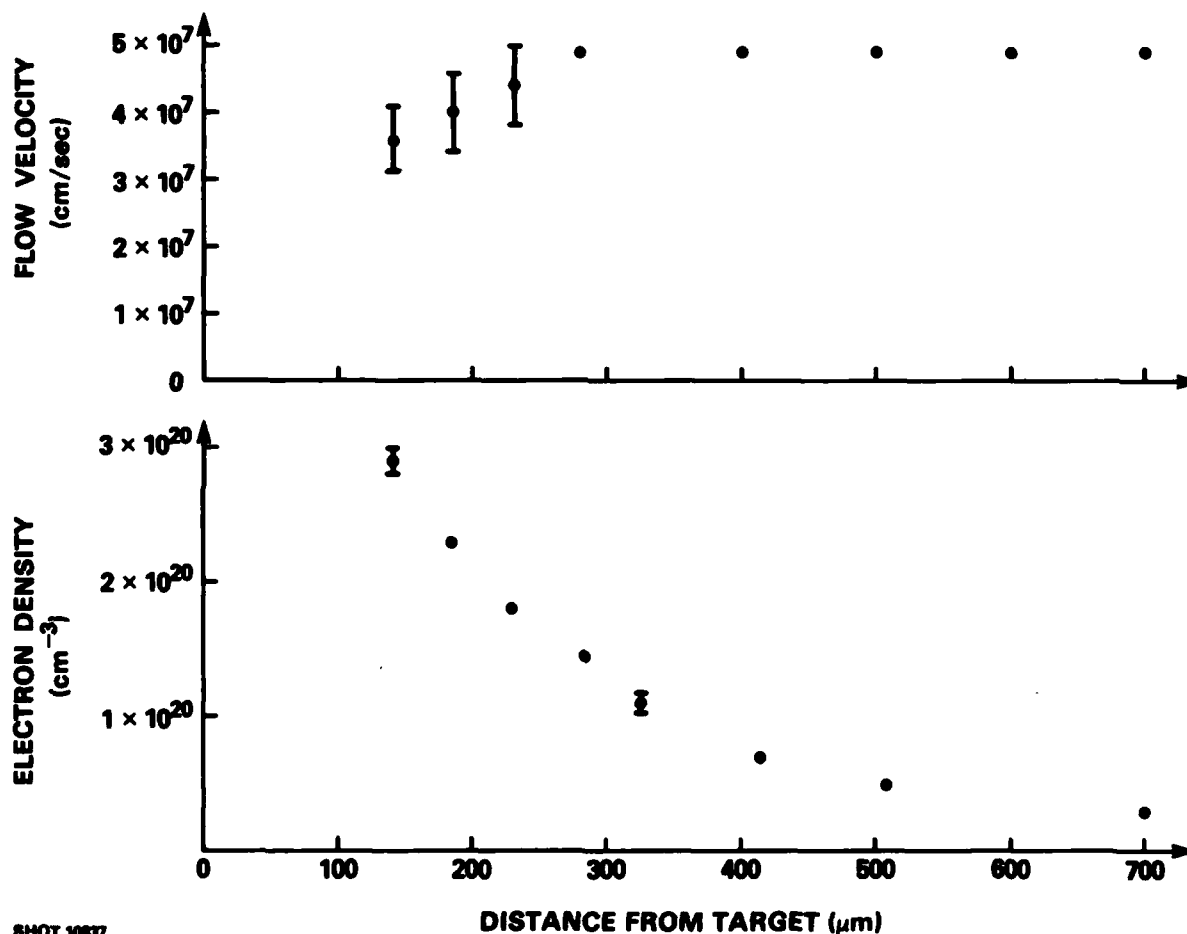
BOUNDARY CONDITION:

v_{∞} FROM TIME-OF-FLIGHT DETECTORS

Fig. 8 — Model for inferring fluid velocity profile.

DENSITY AND FLOW VELOCITY PROFILES BELOW $0.3 n_c$

$E_L = 35 \text{ J}$ $d_{90} \approx 650 \mu\text{m}$ $I_{90} \approx 2 \times 10^{12} \text{ W/cm}^2$ $d_{\text{plasma}} \approx 620 \mu\text{m}$



SHOT 10837

Fig. 9 — Sample of data reduced using model of Fig. 8. Density profile is obtained interferometrically with short-pulse ($\tau_L < 0.5 \text{ ns}$) $3\omega_0$ probing beam.

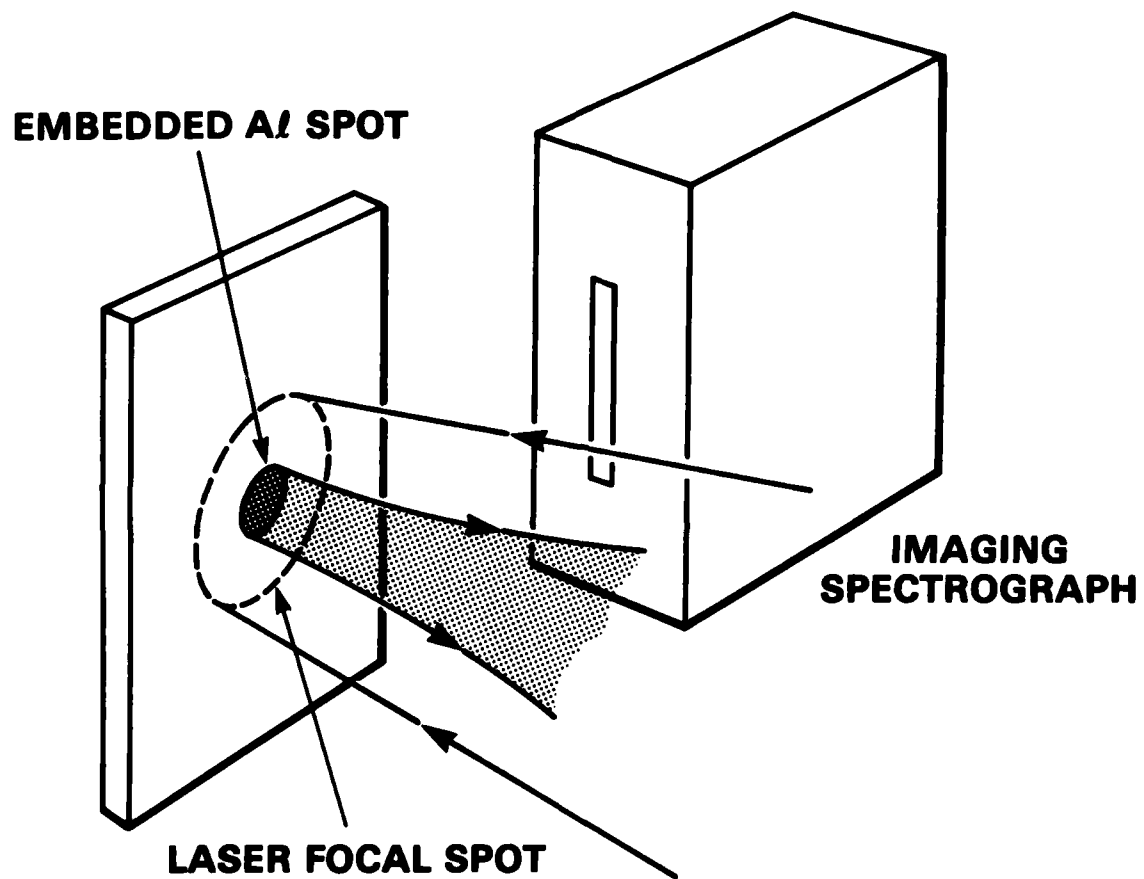


Fig. 10 — Experimental arrangement for spot spectroscopy.

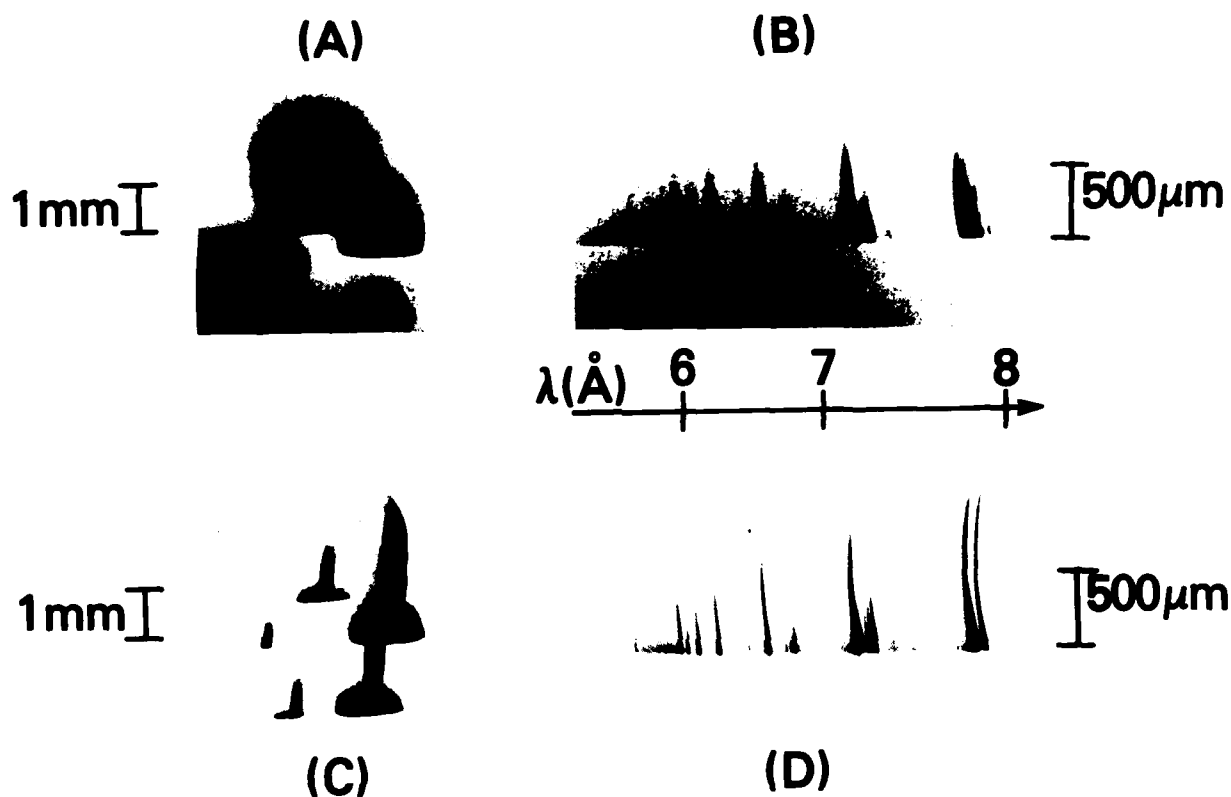
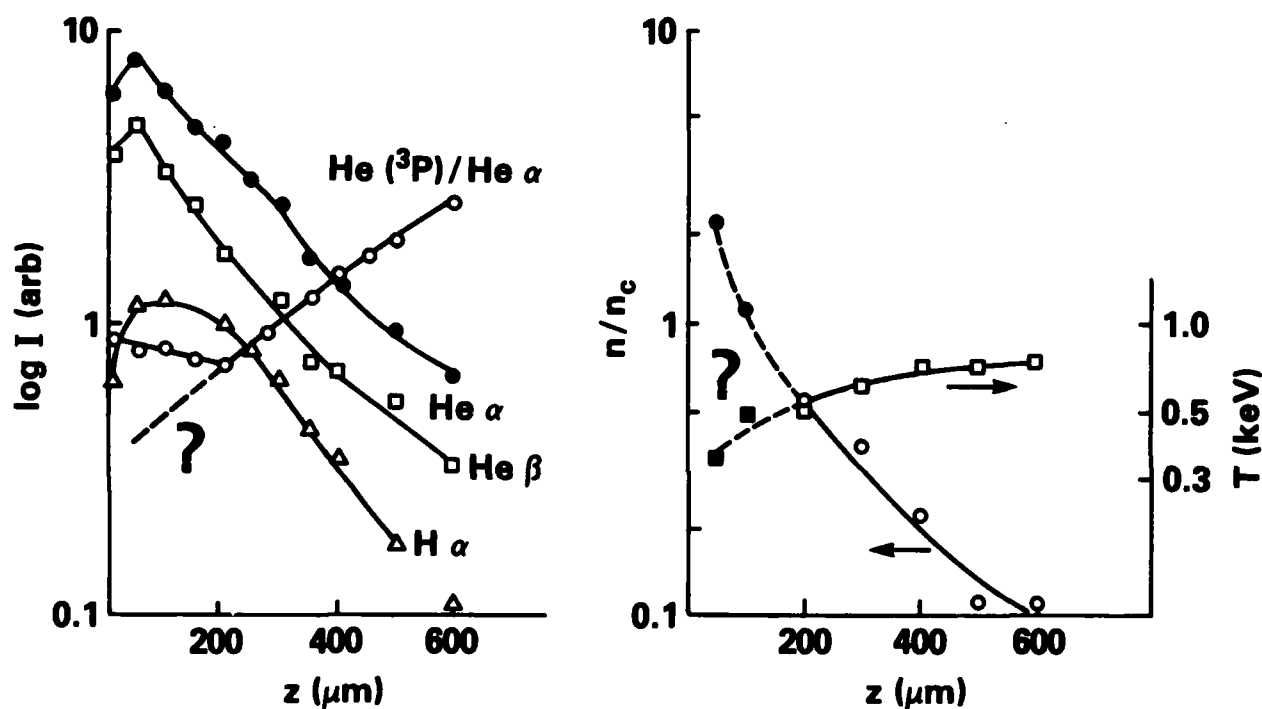


Fig. 11 — Qualitative comparison between data obtained with Al foil target and data acquired using CH plastic target locally embedded with Al. the vertical axis for (A) through (D) corresponds to the laser axis, with the laser incident from above and the target surface at bottom. (A) is obtained with Kodak 3490 film, and (B) through (D) are on Kodak No-Screen Film. (A) X-ray pinhole camera images, obtained with an array of pinholes (5-55 μm diameter), for an Al foil target. Laser intensity $I_0 \approx 3 \times 10^{12} \text{ W/cm}^2$, due to 100 J focused to 1100 μm diameter spot (90% energy content). (B) Spectrum obtained for Al foil target at $I_0 \approx 8 \times 10^{12} \text{ W/cm}^2$, with 110 J focused to 600 μm diameter spot. (C) Pinhole images as in (A), but for CH target embedded with 180 μm diameter Al spot. 225 J of laser energy focused to 900 μm diameter spot yields $I_0 \approx 8 \times 10^{12} \text{ W/cm}^2$. (D) Spectrum from same shot as (C).

n_e AND T_e FROM AI-SPOT SPECTROSCOPY



$$I_{90} \approx 7.3 \times 10^{12} \text{ W/cm}^2 \quad d_{90} \approx 1 \text{ mm} \quad E = 273 \text{ J} \quad \tau_L = 4 \text{ ns} \quad (11505)$$

Fig. 12 — Preliminary reduction of spot spectroscopy data. Left-hand graph shows spatial variation of intensities of He-like α and β lines and of H-like α line, as well as of ratio of He-like intercombination to resonance lines. Right-hand graph shows density and temperature information extracted from line ratios within spectrum. Note that dotted portions of density and temperature profiles are based upon speculative extrapolation of $\text{He } {}^3\text{P}/\text{He } \alpha$ ratio shown in graph at left.

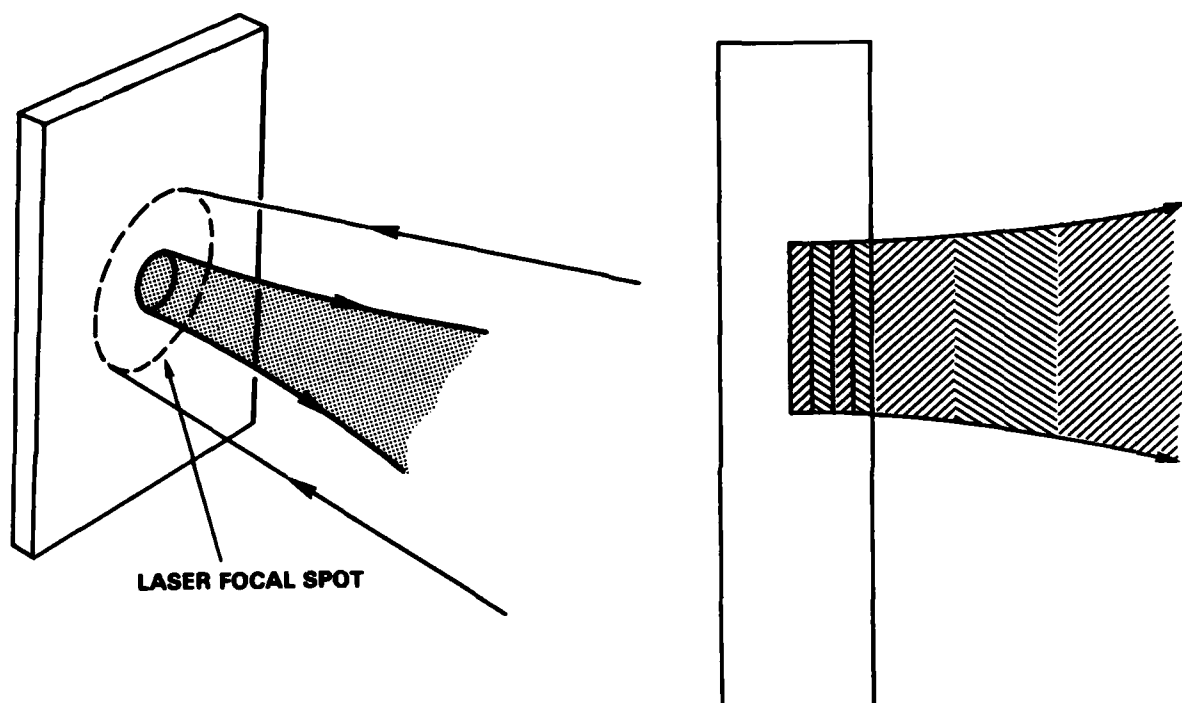


Fig. 13 — New idea for time-resolved measurement of velocity profile. Illustration at left shows that we use laterally localized tracer, as per spot spectroscopy technique. Cross-section of target at right, however, shows that embedded spot is now made of alternating layers of two materials, which ablate sequentially in time during laser irradiation.

STATUS REPORT

I. LONGER-SCALELENGTH EXPTS. UNDERWAY

- **INCREASED BACKSCATTER**
- **DECREASED $2\omega_0$ & HIGH-ENERGY X-RAYS**

II. DIAGNOSTIC DEVELOPMENT CONTINUING

- **FIRST TECHNIQUES FOR V PROFILE**
- **SPOT SPECTROSCOPY FOR n , T**

Fig. 14 — Summary of work-to-date.

END

FILMED